Characterizing the free and surface-coupled vibrations of heated-tip atomic force microscope cantilevers



2014 Nanotechnology 25 345701

(http://iopscience.iop.org/0957-4484/25/34/345701)

IOP Publishing Nanotechnology
Nanotechnology **25** (2014) 345701 (12pp) doi:10.1088/0957-4484/25/34/345701

# Characterizing the free and surface-coupled vibrations of heated-tip atomic force microscope cantilevers*

**Jason P Killgore, Ryan C Tung and Donna C Hurley**

Applied Chemicals and Materials Division, National Institute of Standards and Technology, Boulder, CO 80305, USA

E-mail: killgore@nist.gov

Received 5 March 2014, revised 2 June 2014
Accepted for publication 19 June 2014
Published 6 August 2014

**Abstract**

Combining heated-tip atomic force microscopy (HT-AFM) with quantitative methods for determining surface mechanical properties, such as contact resonance force microscopy, creates an avenue for nanoscale thermomechanical property characterization. For nanomechanical methods that employ an atomic force microscope cantilever's vibrational modes, it is essential to understand how the vibrations of the U-shaped HT-AFM cantilever differ from those of a more traditional rectangular lever, for which analytical techniques are better developed. Here we show, with a combination of finite element analysis (FEA) and experiments, that the HT-AFM cantilever exhibits many more readily-excited vibrational modes over typical AFM frequencies compared to a rectangular cantilever. The arms of U-shaped HT-AFM cantilevers exhibit two distinct forms of flexural vibrations that differ depending on whether the two arms are vibrating in-phase or out-of-phase with one another. The in-phase vibrations are qualitatively similar to flexural vibrations in rectangular cantilevers and generally show larger sensitivity to surface stiffness changes than the out-of-phase vibrations. Vibration types can be identified from their frequency and by considering vibration amplitudes in the horizontal and vertical channels of the AFM at different laser spot positions on the cantilever. For identifying contact resonance vibrational modes, we also consider the sensitivity of the resonant frequencies to a change in applied force and hence to tip–sample contact stiffness. Finally, we assess how existing analytical models can be used to accurately predict contact stiffness from contact-resonance HT-AFM results. A simple two-parameter Euler–Bernoulli beam model provided good agreement with FEA for in-phase modes up to a contact stiffness 500 times the cantilever spring constant. By providing insight into cantilever vibrations and exploring the potential of current analysis techniques, our results lay the groundwork for future use of HT-AFM cantilevers for accurate nanomechanical property measurements.

Keywords: atomic force microscopy, contact resonance, microheater

(Some figures may appear in colour only in the online journal)

## 1. Introduction

Atomic force microscopy (AFM) has shown considerable utility for the nanoscale imaging and spectroscopy of electrical, chemical, thermal and mechanical properties of materials. Mechanical property measurements in particular have garnered much research because of their importance in characterizing structural materials. Significant advances have been made in the accurate determination of room-temperature elastic and viscoelastic properties (e.g., Young's modulus, storage modulus, loss tangent) with the AFM [1–4]. However,

* Publication of NIST, an agency of the US government, not subject to copyright.

 

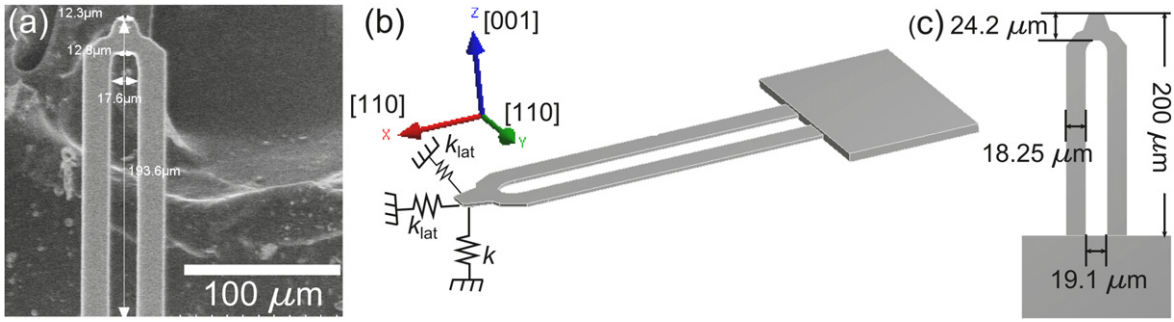


**Figure 1.** (a) Scanning electron micrograph of a commercial HT-AFM probe used as the basis for the finite element model (image provided by K Kjoller, Anasys Instruments). (b) Shaded view of the model used in finite element analysis of the HT-AFM cantilever. (c) Plan view of the cantilever model with dimensions.

the mechanical properties of polymeric nanomaterials depend strongly on temperature, and the temperature dependence of those properties can differ significantly between the macroscale and nanoscale due to localized chemical and confinement effects [5]. Despite a clear need to characterize nanoscale properties as a function of temperature, the evolution of AFM nanomechanical techniques to operate at higher temperatures has been limited [6–8].

Achieving temperature-dependent measurements of mechanical properties requires a means of heating the sample or tip–sample contact, a technique for acquiring raw data from which mechanical properties can be extracted, and analysis methods to translate that raw data into properties. Two primary methods exist to control the temperature of the tip–sample contact in the AFM. Global heating of the entire sample [6, 9] has proven useful for studying nanoscale polymer dynamics, such as observing recrystallization and identifying the glass-transition temperature [9–11]. Key advantages of global sample heating are the ease of measuring and controlling temperature, the ability to observe the specimen in a nearly thermally equilibrated state, and compatibility with most types of commercial cantilevers. Drawbacks to global sample heating are significant thermal drift, possible detrimental interaction with AFM components (e.g., depoling of piezoelectric elements), and slow heating rates due to the time required to reach thermal equilibrium. In addition, the tip–sample contact temperature can be substantially depressed relative to the heater setpoint temperature due to heat transfer to the unheated cantilever and temperature drop though the sample thickness [12]. Finally, when irreversible processes occur (e.g. chemical reactions), a new sample must be prepared to repeat the measurement.

The second approach to control temperature involves local heating of the cantilever tip [13, 14] by integrating a resistive heater into the cantilever. Initially this was achieved with a bent Wollaston wire cantilever, but resolution was limited to micrometer dimensions [13]. Subsequently, advances in microfabrication led to silicon probes with integrated heaters and tip sharpness comparable to traditional AFM probes [14, 15]. Applications of heated-tip AFM (HT-AFM) have included surface manipulation for materials testing [16, 17] and data storage [18], as well as local thermal analysis approaches to identify the softening temperature of materials [13, 19]. To control the current flow and allow the tip to be heated, the cantilevers exhibit a U-shaped geometry (figure 1(a)) with a lower-doped region near the free end of the cantilever. When current is applied, the relatively high resistance of the lightly doped region creates a localized heat source. This HT-AFM method heats only a very small volume of the sample, tip and cantilever. Thus, thermal drift is significantly reduced, extremely high heating rates ($10\,000\ \mathrm{K\ s^{-1}}$) are possible and permanent damage to only a small region of the sample is risked. Careful calibration of the heater temperature and measurement on low-conductivity samples such as polymers allow for precise control of the tip–sample temperature [20, 21]. These advantages compared to global heating make HT-AFM attractive for integration with new dynamic AFM approaches for quantitative property measurement and mapping.

Existing or potential dynamic methods for temperature-dependent measurement of mechanical properties include intermittent-contact modes such as phase imaging [22] and continuous-contact modes such as force modulation (FMM) [23] and contact resonance force microscopy (CR-FM) [24, 25]. The combination of intermittent-contact modes and HT-AFM may be complicated by the complex heat transfer with constantly varying distance between tip and sample. Nonetheless, opportunity does exist for these modes, and studying the free or lightly perturbed vibrations of HT-AFM cantilevers is therefore useful. HT-AFM has thus far been primarily a contact-mode technique, making integration with dynamic contact methods such as CR-FM and FMM more straightforward.

Indeed, much of the recent interest on dynamic AFM with HT-AFM cantilevers has utilized the surface-coupled CR-FM vibrations of the cantilever [7, 8, 26]. Combining CR-FM and HT-AFM was first demonstrated by Jesse *et al* [7, 8]. A major innovation of their work involved a multistep heating process to 'freeze in' the contact area. The tip was brought in contact, heated above the softening temperature of the polymer sample and then cooled. Measurements of the resonance frequency and quality factor of the vibrating cantilever in contact were then performed with the tip heated to a slightly lower temperature. By proactively creating a very large contact area, the heated measurement became much less susceptible to viscoelastic creep effects. Additional progress

involved improvements in HT-AFM cantilever actuation. Lee *et al* positioned a focused magnet near the cantilever to induce a very clean Lorentz driving force without the spurious system vibrations that can complicate acoustic excitation [26]. By applying the Lorentz force drive to CR-FM, the authors found that transition temperatures of thermosetting polymeric materials could be more readily measured than with quasistatic HT-AFM techniques.

Here, we analyze the mechanical vibrations of commercially available HT-AFM cantilevers. Previous work characterized the quasistatic mechanical properties of HT-AFM cantilevers, but did not delve substantially into the cantilever vibrations [27]. We show with finite element analysis (FEA) that the U-shape of the cantilever results in several vibrational modes that do not exist in rectangular cantilevers. These vibrational modes can interact with one another, introducing new challenges for quantitative analysis of results from dynamic AFM experiments. Experimental free and contact-resonance spectra confirm that many of these modes are excited with a single excitation direction. Because of the large number of modes excited, identification of the desired versus undesired modes for analysis becomes more challenging. To this end, we investigate how laser position and measurement of both horizontal and vertical photodiode channels can be used to more confidently identify a mode type in free space and in surface-coupled contact. By varying the force setpoint, the sensitivity of different mode types to changes in contact stiffness is evaluated. Finally, we evaluate the applicability of analytical models based on Euler–Bernoulli beam theory for quantitative contact stiffness measurements from CR-FM with HT-AFM cantilevers. The results pave the way for temperature-dependent nanoscale measurements of mechanical properties with HT-AFM.

## 2. Methods[1]

### 2.1. Experimental details

Experimental measurements of cantilever vibrations were performed on a Cypher AFM (Asylum Research/Oxford Instruments, Santa Barbara, CA) with a commercially available HT-AFM cantilever (AN-200, Anasys Instruments, Santa Barbara, CA). The nominal spring constant of the cantilever is between 0.5 N m$^{-1}$ and 3.0 N m$^{-1}$. For both free and contact vibrations, actuation was achieved normal to the sample surface by means of a broadband piezoelectric actuator (Contact Resonance Sample Actuator, Asylum Research/Oxford Instrument, Santa Barbara, CA) located beneath the sample. The commercially available actuator has a strongly damped resonance which provides a nearly flat frequency response in the range of the experiment, with no undesirable spurious peaks. Free-space vibrations were characterized with the cantilever located ~3.5 $\mu$m from the sample surface so that the actuator vibration can couple through the air. Surface-coupled (contact mode) vibrations were characterized with the tip in stationary contact with a glass microscope slide at deflections of 50 nm and 150 nm. At each deflection setpoint, the excitation frequency of the actuator was swept from 100.0 Hz to 4.0 MHz at constant drive voltage while a lock-in amplifier measured the vibration amplitude of the cantilever. To differentiate the types of vibrations, the dynamic response in both the vertical and horizontal photodetector channels was sequentially measured. This process was performed for two different locations of the laser on the cantilever.

### 2.2. Simulation

FEA of the HT-AFM cantilever's vibrational modes was performed with the modal analysis function in a commercial FEA software (Ansys Workbench, Cecil Township, PA) package. The HT-AFM geometry was modeled in commercial CAD software (Autodesk Inventor, San Rafael, CA) based on manufacturer specifications and dimensions obtained from scanning electron microscopy images such as the one shown in figure 1(a). Because experimental cantilevers will exhibit significant geometric variation between and within batches, it was not the intent to exactly model a single experimental cantilever, but rather to model one with representative dimensions. Due to the difficulty of direct measurement, the thickness dimension was used as an adjustable parameter that was varied until the simulated fundamental resonance frequency was within 100 Hz of its experimental counterpart. A resultant thickness of 1.9 $\mu$m was determined. The silicon cantilever was modeled as orthotropically elastic with the crystallographic orientations indicated in figure 1(b), and dimensions as shown in figure 1(c). The rotated elastic parameters were Young's moduli $E_x = E_y = 169.7$ GPa, $E_z = 130.4$ GPa, Poisson's ratios $\nu_{xz} = \nu_{yz} = 0.362$, $\nu_{zy} = \nu_{zx} = 0.278$, $\nu_{xy} = \nu_{yx} = 0.061$, and shear moduli $G_{xz} = G_{yz} = 80$ GPa, $G_{xy} = 51$ GPa [28]. The density $\rho$ was set to 2330 kg m$^{-3}$. No modifications to the material properties were made to account for potential differences in mechanical properties in regions of the cantilever with different doping levels. The system was tetrahedrally automeshed with ten-node 3D elements, resulting in 25 527 nodes and 12 427 elements. A convergence study showed a maximum change in frequency of 0.23% for any of the first 15 free resonant modes of the cantilever when the meshing density was doubled, and thus the above mesh was considered an adequate compromise of speed and accuracy.

In our model, the cantilever was rigidly clamped at two pads near the cantilever base to represent the coupling present on a large, rigid silicon chip. The tip was modeled as a 4 $\mu$m tall square protrusion with base dimensions and orientation comparable to the experimental tip. This geometry avoids the very small element size and increased computational complexity that would arise if the tip were modeled with the nanometer sharpness of an actual cantilever, while still providing a comparable moment arm as a pyramidal tip. Tip-

[1] Certain commercial equipment, instruments or materials are identified in this paper in order to specify the experimental procedure adequately. Such identification does not imply recommendation or endorsement by NIST, nor does it imply that the materials or equipment identified are necessarily the best available for the purpose.

sample coupling was simulated by three orthogonal springs oriented to represent the 11.5° approach angle of the experimental AFM setup. Because contact is represented by linear springs rather than a true tip–sample interaction (e.g., Hertz or Derjaguin–Müller–Toporov), the simplified tip geometry described above is not expected to significantly influence beam dynamics. The contact stiffness $k$ in the surface normal direction was varied from 0.2 times to 10 000 times the cantilever's flexural spring constant $k_L$. The value of $k_L = 1.45\ \mathrm{N\ m^{-1}}$ was determined from a static FEA simulation of cantilever displacement when a 1 nN load was applied normal to the tip. The two lateral springs oriented in plane with the hypothetical sample surface were given stiffness $k_{lat} = 0.9k$, approximating an isotropic sample with Poisson's ratio $\nu = 0.2$ [29]. A large range of contact stiffness was investigated to encompass scenarios ranging from light contact on compliant materials to the large contact areas created by the freeze-in method [7, 8] described in the introduction.

## 3. Results and discussion

### 3.1. Free vibration

Figure 2 shows FEA solutions of the HT-AFM cantilever's free vibrational modes in the frequency range from 0.0 MHz to 4.0 MHz. A total of 13 modes are observed in this frequency range. Due to the more complex geometry of the HT-AFM cantilever, more vibrational modes are available across typical AFM frequencies compared to rectangular cantilevers with comparable spring constant. The modes depicted in figures 2(a), (c), (f), (h) and (l) exhibit in-phase motion of the cantilever's parallel arms and represent the first five in-phase flexural (*ipF*) modes of the cantilever, respectively. At successively higher flexural modes, the FEA model predicts an increased contribution of anticlastic curvature (i.e., curvature perpendicular to the main flexural axis, but with opposite sign) towards the overall mode shape compared to that observed for rectangular cantilevers. This is attributed to the coupling between the two arms and overall more plate-like geometry of the lever compared to a long, slender rectangular lever. Nonetheless, the normalized frequencies of the free *ipF* mode, that is, the frequencies relative to that of the fundamental *ipF* mode differ by only a small amount from those predicted with Euler–Bernoulli beam theory for rectangular cantilevers. For a single cantilevered beam with constant cross section, the flexural resonance frequency $f_n^{0\text{-F}}$ in free space of the $n$th flexural mode relative to that of the lowest mode ($n = 1$) is given by

$$\frac{f_n^{0-\mathrm{F}}}{f_1^{0-\mathrm{F}}} = \left(\frac{\lambda_n^0 L}{\lambda_1^0 L}\right)^2, \tag{1}$$

where $\lambda_n^0 L$ is the $n$th root of the equation

$$1 + \cos\left(\lambda_n^0 L\right)\cosh\left(\lambda_n^0 L\right) = 0. \tag{2}$$

For the first five flexural resonances, this gives theoretical normalized frequencies $f_n^{0\text{-F}}/f_1^{0\text{-F}} = [1,\ 6.27,\ 17.55,\ 34.39,\ 56.84]$, respectively. FEA predicts normalized frequencies $f_n^{0\text{-}ipF}/f_1^{0\text{-}ipF} = [1,\ 6.25,\ 17.35,\ 33.31,\ 54.29]$ for the first five *ipF* flexural modes of the HT-AFM cantilever, respectively. The discrepancy in normalized frequencies between the Euler–Bernoulli model and the FEA is generally small but increases with mode number. For the fifth *ipF* mode, the discrepancy is approximately 4.5%.

After the flexural modes, the next most frequent mode type is shown in figures 2(b), (d), (g), and (k). Here, the modes exhibit out-of-phase flexural (*opF*) motion of the individual cantilever arms, which induces a pronounced torsional motion of the tip. The normalized frequencies of the first four *opF* free modes are predicted at $f_n^{0\text{-}opF}/f_1^{0\text{-}ipF} = [4.99,\ 10.68,\ 23.13,\ 45.46]$, respectively. It is interesting to note that the *opF* modes are excited by actuation in the same direction as the *ipF* modes, but because of the tip motion, these modes could be used to probe shear or frictional mechanical properties. This is potentially useful from a nanomechanics standpoint and contrasts with earlier torsional AFM methods that required customized shear or rotational actuation [30]. These modes should also be considered in tapping-mode operation, where the near-integer spacing ($f_1^{0\text{-}opF}/f_1^{0\text{-}ipF} = 4.99$) of the resonance frequencies means that the first out-of-phase mode could be excited by energy from the fifth harmonic of $f_1^{0\text{-}ipF}$ during the nonlinear force–distance portion of a near-surface oscillation. This coupled motion would include normal and shear interaction between the tip and sample, and could complicate quantitative analysis. The in-phase and out-of-phase lateral resonances are shown in figures 2(e) and (m) and occur at normalized frequencies $f_1^{0\text{-}ipL}/f_1^{0\text{-}ipF} = 14.39$ and $f_1^{0\text{-}opL}/f_1^{0\text{-}ipF} = 54.64$, respectively. The remaining predicted modes in the frequency window are shown in figures 2(i) and (j), and represent symmetric *sP* and antisymmetric *aP* plate modes, respectively.

For comparison with the FEA results, figures 3(a) and (b) show the experimental free resonance spectra for the vertical (V) and horizontal (H) photodiode channels at laser positions A and B indicated by the respective insets. Position A was expected to highlight the motion of the individual arm, while position B would accentuate the motion of the connecting bar in the vicinity of the tip. It was not expected that the FEA and experiments would agree perfectly, because of simplifications to the FEA geometry and uncertainty in the dimensional measurements. Furthermore, some of the vibrational modes depicted in figure 2 could be difficult to excite or detect because of their high dynamic stiffness, orientation relative to the normal drive force and small response amplitude in either the flexural or torsional direction. Nonetheless, 11 different resonance peaks were experimentally observed with the acoustic excitation normal to the sample surface.

Table 1 lists the frequencies of the observed modes in ascending order and compares them to the normalized frequencies predicted by FEA. The rank ordering and approximate frequencies of the peaks provide immediate clues to the identities of the modes. The first three *ipF* and *opF* modes show <2% discrepancy between experiment and simulation. The higher *ipF* and *opF* modes show discrepancy between

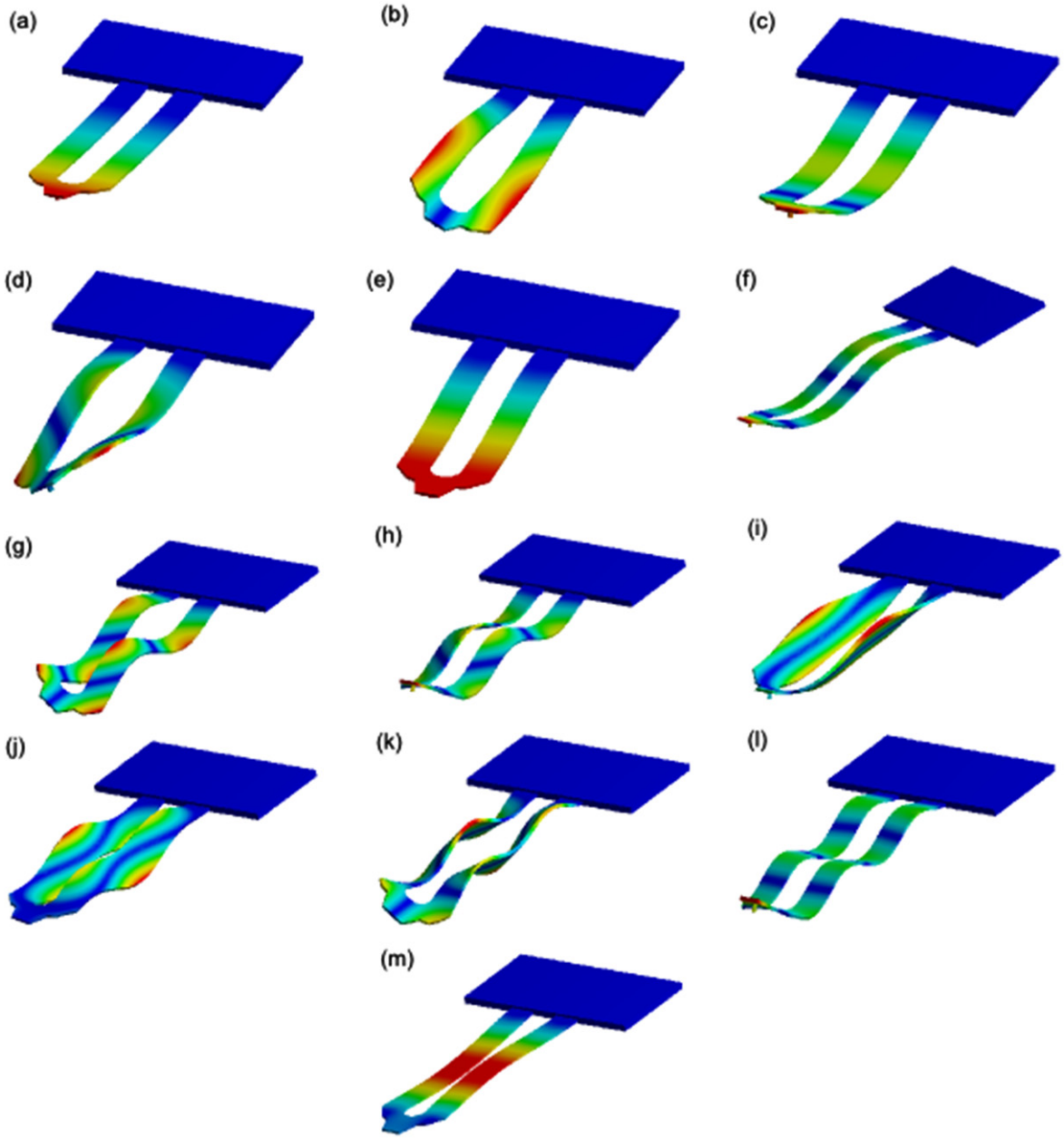


**Figure 2.** FEA mode shape analysis for the first 13 free modes of the HT-AFM cantilever. Color scale indicates magnitude of vibration amplitude of the element relative to the static cantilever (red = maximum amplitude, blue = 0). Specific modes observed are (a) first in-phase flexural $f_1^{0\text{-}ipF}$, (b) first out-of-phase flexural $f_1^{0\text{-}opF}$, (c) second in-phase flexural $f_2^{0\text{-}ipF}$, (d) second out-of-phase flexural $f_2^{0\text{-}opF}$, (e) first in-phase lateral $f_1^{0\text{-}ipL}$, (f) third in-phase flexural $f_3^{0\text{-}ipF}$, (g) third out-of-phase flexural $f_3^{0\text{-}opF}$, (h) fourth in-phase flexural $f_4^{0\text{-}ipF}$ (i) symmetric plate mode $f_1^{0\text{-}sP}$, (j) antisymmetric plate mode $f_1^{0\text{-}aP}$, (k) fourth out-of-phase flexural $f_4^{0\text{-}opF}$, (l) fifth in-phase flexural $f_5^{0\text{-}ipF}$, and (m) first out-of-phase lateral $f_1^{0\text{-}opL}$.

2% and 8%. Larger discrepancy for the higher modes may correspond to an increased dependence on the precise shape of the coupling segment between the cantilever arms. The non-*ipF* and non-*opF* modes show varying detectability and agreement with simulation. It was determined that the symmetric plate mode and the out-of-phase lateral mode could not be detected with the investigated experimental set-up. The asymmetric plate mode exhibited 6% discrepancy between mode and experiments, while the poorest agreement for a detected mode was a 22% discrepancy for the in-phase lateral mode.

By considering the resonant mode shapes from FEA and the relative amplitudes of the experimental resonance peaks in the vertical and horizontal channels for either laser position, characteristics of the detection can be correlated with the mode shapes for eventual use interpreting surface coupled data. The absolute amplitude of any peak is influenced by the frequency dependence of the photodetector and the sample actuator as well as the local slope of the eigenmode in the detected channel. The *ipF* modes show dominant response in the vertical V channel, relative to the horizontal H channel, regardless of laser position. For position B, the first *ipF* mode

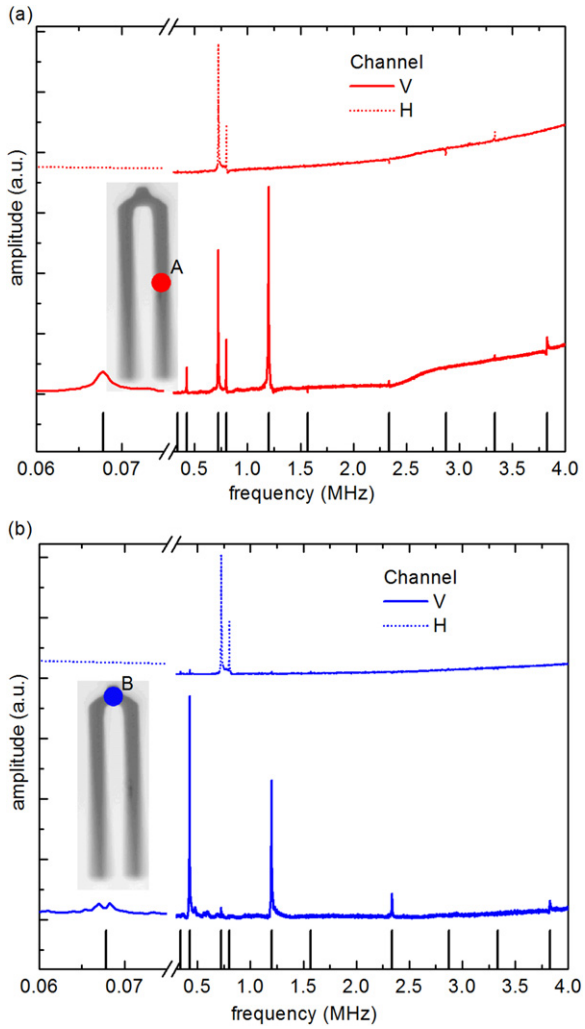


**Figure 3.** Acoustically driven free-resonance spectra of the HT-AFM cantilever showing both vertical V and horizontal H photodiode channels with laser at positions A and B for (a) and (b), respectively. The black vertical lines indicate a likely resonant frequency determined from one or more of the channels or positions. Inset optical micrographs show approximate laser positions. The *x*-axis has been split to improve clarity and avoid regions without resonances.

shows a low amplitude peak, with evidence of noise that is not apparent for position A. This low-quality peak at position B is attributed to the weak excitation energy of the sample actuator at low roll-off frequencies combined with poorer optical sensitivity of the lever compared to position A. Position A provides improved detection of all peaks except the second and fourth *ipF* modes, where position A is near an antinode of the mode shape. In general, the *opF* modes show strong response in the H channel for most mode numbers and laser positions. In some cases, such as laser position A for $f_2^{0\text{-}opF}$, there is also a substantial vertical component due to the local mode shape. The trends in the observed detectability of the modes will also inform the characterization of contact resonance mode shapes, but it must be understood that the locations of nodes and antinodes will change as the boundary conditions are stiffened.

### *3.2. Surface-coupled vibrations*

Similar to the characterization procedure for the free modes, a combination of FEA and experiments was used to characterize the modal behaviors in surface-coupled contact. Figure 4(a) shows a plot of contact resonance frequency versus normalized contact stiffness $\alpha = k/k_L$, determined from FEA. Many of the modes cross or veer as a function of $\alpha$, requiring assessment of the mode shape at each boundary condition rather than simple correlation of the rank order of the frequencies of the modes. This crossing behavior can also create experimental complications where the highest-amplitude eigenmode jumps between two modes as a subtle function of contact stiffness and mode shape in a very narrow frequency window. This creates a challenge for resonant frequency tracking, as well as mode identification.

In CR-FM, it is desirable to maximize the frequency sensitivity (i.e., the increase in frequency for a given increase in contact stiffness) of the utilized eigenmode(s) for the range of contact stiffness under investigation. Ideally, a single resonant mode would show high and uniform frequency sensitivity across all values of $\alpha$. In reality, a given mode is sufficiently sensitive only over a finite range of stiffness in the vicinity of the dynamic stiffness of the mode. Figures 4(b)–(d) indicate the shift in frequency from free space to the specified contact stiffness for (b) the first five *ipF* modes, (c) the first four *opF* modes, and (d) other modes of the cantilever. The most sensitive modes may shift as much as 1 MHz in the stiffness range of the simulation, whereas the less sensitive modes show shifts of less than 10 kHz. These stiffness-insensitive modes include the first and second *opF* resonances, the plate modes, and the *opL* resonance. These modes are insensitive to sample stiffness either because they induce very little motion of the tip or because the stiffness of the eigenmode is much greater than the contact stiffness in the probed direction. In contrast to the first and second *opF* modes, the third and fourth *opF* modes show more pronounced increases in frequency with increased contact stiffness. Another high-sensitivity mode is the first in-phase lateral *ipL* mode of the cantilever. This mode primarily probes the in-plane stiffness of the contact, giving it similar utility as the *opF* modes for probing shear properties of a surface; however, its most sensitive stiffness-regime is lower than for the *opF* modes.

Most contact resonance experiments with conventional cantilevers focus on pure flexural modes. For the HT-AFM cantilever, figure 4(a) shows that the *ipF* modes exhibit 'S-curve' [31] behavior that is qualitatively similar to that exhibited by rectangular cantilevers. The resonant frequency of an eigenmode increases steadily with increasing contact stiffness until the contact becomes much more rigid than the dynamic spring constant of the eigenmode, at which point the frequency plateaus. As shown in figure 4(b), the value of $\alpha$ at which the plateau occurs increases with increasing mode number $n$. Thus by the careful use and choice of different modes, a wide range of contact stiffness can be sensitively probed with a single cantilever.

**Table 1.** Summary of FEA results and experimental free-vibration data. V and H denote vertical and horizontal channels, respectively. 'Dip' denotes a depression in the spectrum instead of a peak.

| | | | | | Amplitude (mV) | | | |
|---|---|---|---|---|---|---|---|---|
| | | | | | Position A | | Position B | |
| Mode # | Mode description | $f/f_1^{0\text{-}ipF}$ (FEA) | $f$ (kHz) (exp.) | $f/f_1^{0\text{-}ipF}$ (exp.) | V | H | V | H |
| 1 | $f_1^{0\text{-}ipF}$ | 1 | 67.8 | 1 | 2.4 | 0 | 0.6 | 0 |
| 2 | $f_1^{0\text{-}opF}$ | 4.98 | 338.6 | 4.99 | 0 | 0.3 | 0.1 | 0 |
| 3 | $f_2^{0\text{-}ipF}$ | 6.25 | 428.0 | 6.31 | 3.1 | 0 | 13.0 | 0.3 |
| 4 | $f_2^{0\text{-}opF}$ | 10.68 | 724.9 | 10.69 | 16.2 | 15.4 | 0.6 | 6.9 |
| 5 | $f_1^{0\text{-}ipL}$ | 14.39 | 800.6 | 11.81 | 6.1 | 5.3 | 0 | 3.3 |
| 6 | $f_3^{0\text{-}ipF}$ | 17.35 | 1200.4 | 17.7 | 23.9 | Dip | 8.4 | 0.2 |
| 7 | $f_3^{0\text{-}opF}$ | 23.13 | 1569.4 | 23.14 | Dip | 0.2 | 0 | 0.1 |
| 8 | $f_4^{0\text{-}ipF}$ | 33.31 | 2337.4 | 34.47 | 0.6 | Dip | 1.4 | 0 |
| 9 | $f_1^{0\text{-}sP}$ | 35.98 | | (not observed experimentally) | | | | |
| 10 | $f_1^{0\text{-}aP}$ | 39.77 | 2871.1 | 42.34 | 0 | Dip | 0 | 0 |
| 11 | $f_4^{0\text{-}opF}$ | 45.46 | 3333.4 | 49.16 | 0.4 | 1.1 | 0 | 0 |
| 12 | $f_5^{0\text{-}ipF}$ | 54.29 | 3826.6 | 56.43 | 1.7 | 0.2 | 0 | 0 |
| 13 | $f_1^{0\text{-}opL}$ | 54.64 | | (not observed experimentally) | | | | |

Because so many of the modes induce in-plane motion of the tip, which acts on the sample through the moment arm of the tip, the precise values of the lateral stiffness and tip height $h$ must be considered. Figure 5 shows the relative change in contact resonance frequency as the tip height is varied from 3 $\mu$m to 6 $\mu$m, which is the cantilever manufacturer's specified range. Results are shown for three different values of normalized contact stiffness: (a) $\alpha = 10$, (b) $\alpha = 100$, and (c) $\alpha = 1000$. As contact stiffness is increased, the influence of the tip height on contact resonance frequencies increases substantially. The influence of the relative changes in frequency on accurately correlating frequency to contact stiffness must be considered in light of the frequency sensitivity of a mode in the contact stiffness regime under investigation. For instance, a 1 kHz frequency uncertainty from tip height is more important for a mode that has plateaued in frequency than a mode at its optimal contact stiffness for highest frequency sensitivity. Thus, tip height effects are very important for the *opF* modes at all contact stiffnesses but are significant for the *ipF* modes only when the contact stiffness is much higher than the dynamic stiffness of that eigenmode. It should also be noted that the FEA assumes a linear interaction of the lateral springs, whereas experimentally it may be possible for the tip to slide against a substrate. In the latter case, the friction force between the tip and sample will result in a complex lateral stiffness that is generally much smaller than one would expect from the shear modulus of the material. To avoid this effect, sample excitation amplitudes may need to be kept very small.

Figure 6(a) shows representative experimental contact spectra for the HT-AFM cantilever with a DC cantilever deflection of 150 nm and the laser located at position B. Similar to the free spectra, 11 peaks are observed in contact, although the fourth and fifth peaks are believed to be a split peak of a single eigenmode. Identification of the contact resonance peaks is considerably more challenging than for free modes, because the expected ordering of the peaks as a function of contact stiffness is not precisely known. We attempted to identify the modes on the basis of their frequency, the relative amplitudes in the V and H channels for both laser positions and the observed shifts in frequency that occur as deflection setpoint is increased (i.e., the frequency sensitivity). Figure 6(b) shows the ratio $A_V/A_H$ of the vertical and horizontal amplitudes for laser positions A and B. Values of $A_V/A_H > 1$ indicate a dominant peak in the V channel, whereas values of $A_V/A_H < 1$ indicate a dominant peak in the H channel. These results are complemented by the lighter shaded bars in figure 6(c), which show the percent increase in frequency as the deflection setpoint was increased from $d = 50$ nm to $d = 150$ nm.

Because the contact *ipF c-ipF* resonances are generally bracketed by their corresponding and next-highest free resonance frequencies, their ranges are limited. From free space and FEA results, we expect that the *ipF* modes will be evidenced by dominant peaks in the V channel for at least one laser position and typically larger frequency sensitivity than the non-*ipF* modes. From these criteria we identify the first, fourth and fifth, seventh, and eighth experimental peaks as the modes at $f_1^{c\text{-}ipF}$, $f_2^{c\text{-}ipF}$ (split peak), $f_3^{c\text{-}ipF}$, and $f_4^{c\text{-}ipF}$, respectively. Surprisingly, the mode identified as $f_4^{c\text{-}ipF}$ shows a dominant horizontal peak at laser position A. Interference with an antinode was observed for $f_4^{0\text{-}ipF}$ in free space with position A, which suggests that position A is still near an antinode when in contact. This result further underlines the importance of optimized laser positioning when operating with HT-AFM cantilevers. In terms of absolute and percentage frequency shift, the highest frequency sensitivities in the contact stiffness range under investigation were exhibited for $f_3^{c\text{-}ipF}$ and $f_4^{c\text{-}ipF}$. For a more compliant sample, a lower eigenmode might have the highest sensitivity; the optimum mode in that case could still be determined using the force-varying approach applied here.

The *c-opF* out-of-phase contact resonances were identified based on their dominant horizontal channel response at

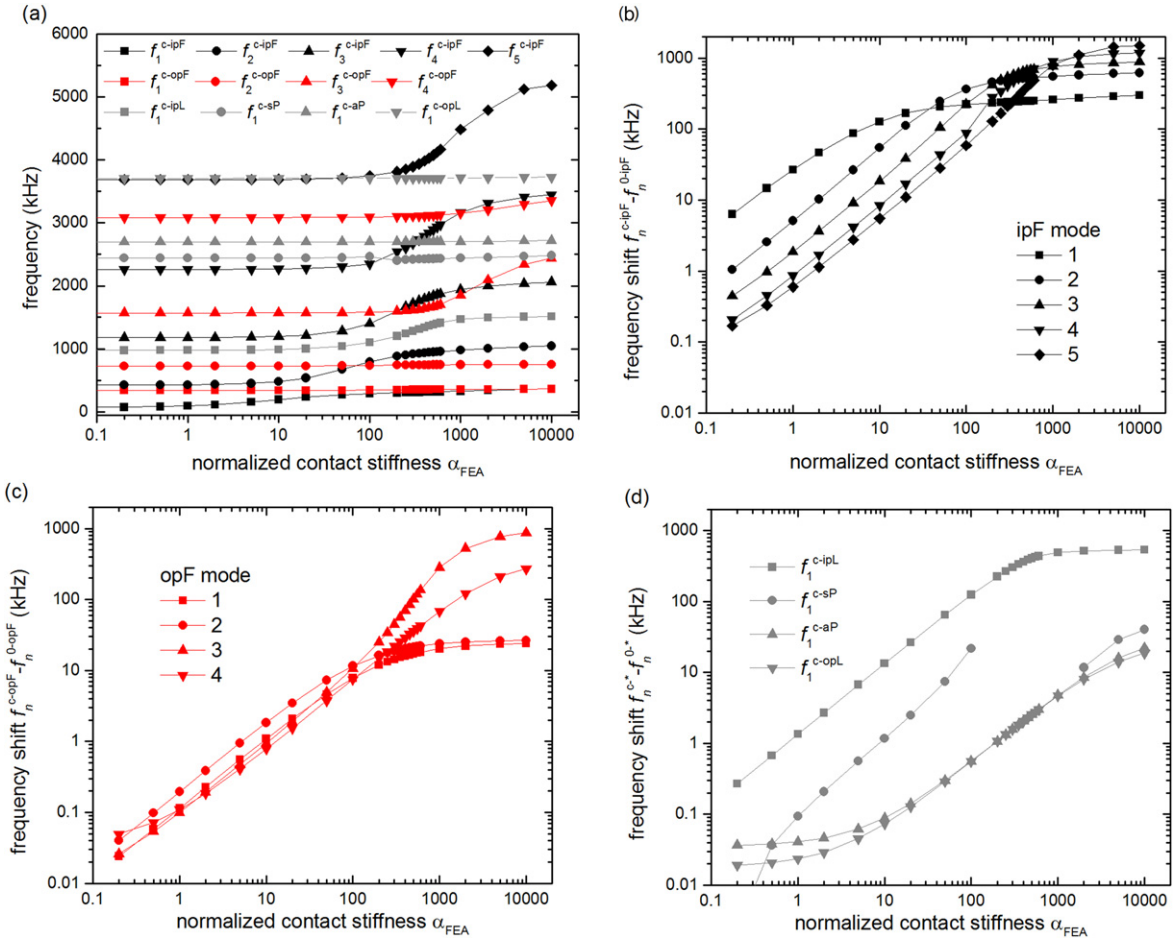


**Figure 4.** (a) Contact resonance frequencies of the first 13 HT-AFM cantilever eigenmodes predicted by FEA versus normalized contact stiffness $\alpha_{FEA}$. The in-phase flexural modes are denoted *c-ipF*, the out-of-phase flexural modes are denoted *c-opF*, the in-phase lateral mode is denoted *c-ipL*, the out-of-phase lateral mode is denoted *c-opL* and the symmetric and antisymmetric plate modes are denoted *c-sP* and *c-aP*, respectively. (b), (c) and (d) show the shift in frequency from an eigenmode's free frequency to its contact resonance frequency as a function of $\alpha_{FEA}$ for the in-phase flexural, out-of-phase flexural, and other modes, respectively.

laser position B and their close frequency proximity to a corresponding free *opF* peak. The second, third, sixth, and eleventh experimental peaks were assigned to the modes at $f_1^{c\text{-}opF}$, $f_2^{c\text{-}opF}$, $f_3^{c\text{-}opF}$, and $f_4^{c\text{-}opF}$ respectively. These modes show more than an order of magnitude lower frequency sensitivity than the most sensitive *ipF* modes at these setpoints. Nonetheless, positive frequency shifts could be identified when load was increased, and the ability of these modes to probe in-plane properties remains a viable application area. Mode 10 was assigned to the antisymmetric plate mode. Mode 9 was assigned to the symmetric plate mode, which was not detected in free space but predicted by FEA to fall slightly below the frequency of the *aP* mode.

After a mode was identified, we assessed how much the frequency increased in contact relative to the corresponding free frequency, as shown by the dark bars in figure 6(c). A large frequency shift from free space to contact, in conjunction with a small frequency shift between the two deflection setpoints, indicates that the mode is nearly pinned (e.g., the first *ipF* resonance $f_1^{c\text{-}ipF}$). Although such modes may provide some sensitivity to mechanical-property differences between different materials or the same material at different temperatures, the magnitude of the frequency shift will be much lower than for the higher *ipF* modes. Consistent with the FEA, the first two *c-opF* frequencies increased only slightly from free space to contact. The third *c-opF* frequency also showed minimal frequency increase from free to contact; however FEA predicts that in a higher-stiffness regime, this mode would become more sensitive.

Overall, these results emphasize the significance and difficulties of accurately identifying the excited modes for CR-FM as well as the potential benefits of operating with the most sensitive eigenmodes. Selectively identifying and ultimately tracking the more widely-used *ipF* modes requires careful positioning of the laser spot. Ultimately, it may prove beneficial to capture a signal proportional to $A_V/A_H$ during scanning to ensure that the desired *ipF* modes are tracked without jumping to an *opF* peak.

### 3.3. Analytical models to describe HT-AFM contact stiffness

Although FEA is attractive for lending insight into the types of modes and their relative frequencies, batch variations among individual cantilevers make FEA a limited tool for

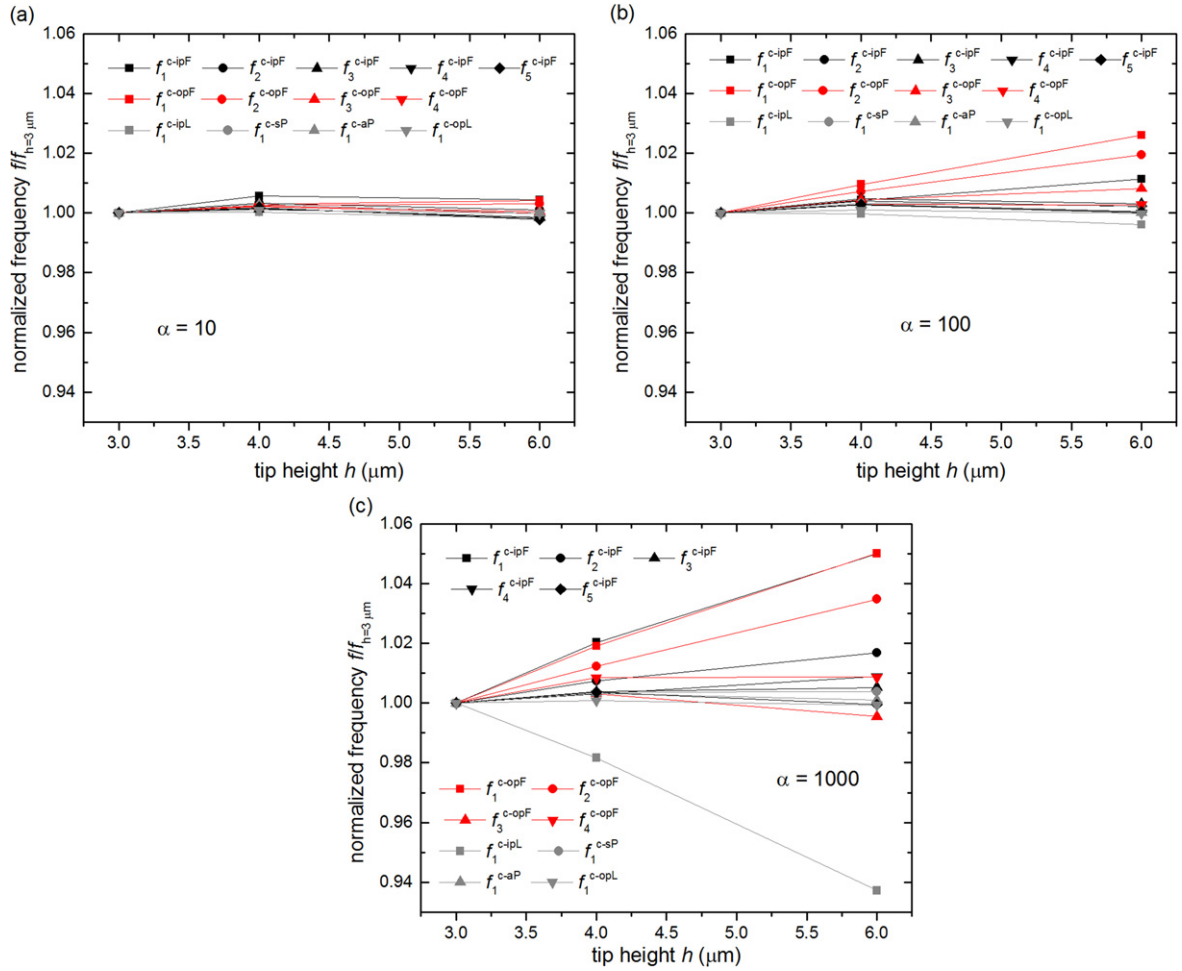


**Figure 5.** Normalized change in contact resonance frequency as tip height is increased from 3 $\mu$m to 4 $\mu$m to 6 $\mu$m for contact stiffnesses of (a) $\alpha = 10$, (b) $\alpha = 100$ and (c) $\alpha = 1000$.

analyzing routine AFM measurements. The end goal is to find the simplest beam model, with the fewest parameters, that adequately describes the more complex geometry or boundary conditions modeled in FEA to represent the real cantilever. Although researchers have recently derived a model capable of predicting in-phase and *opF* free resonance frequencies of the HT-AFM cantilevers [32], the model was not extended to surface-coupled vibrations. Because of their relation to the flexural modes of rectangular cantilevers, only the *ipF* vibrations were modeled below. The general premise is to simulate the data produced in CR-FM experiments using the free and surface-coupled frequency results from FEA models with prescribed contact stiffness $k_{FEA}$. We then compare the values of contact stiffness calculated with Euler–Bernoulli beam theory to the values used in the FEA simulation. For rectangular cantilevers, it was previously shown that the behavior of commercial rectangular cantilevers is well described under many conditions by what we call the simple analytical model (SAM) [33]. As indicated by figure 7(a), the model consists of a beam oriented parallel to the sample surface, with a spring representing the tip–sample contact located at some location along the cantilever's length. Here, we apply a similar methodology as [33] to the U-shaped HT-AFM cantilevers. The normalized contact stiffness $\alpha_{SAM}$ of the flexural modes is given by

$$\alpha_{SAM} = \frac{k_{SAM}}{k_L} = \frac{2}{3}(\lambda_n L\gamma)^3 \frac{\left(1 + \cos\lambda_n L \cosh\lambda_n L\right)}{D}, \quad (3)$$

where $k_{SAM}$ is the stiffness of the normal spring, $k_L$ is the spring constant of the cantilever and $\gamma$ is the location of the tip along the lever normalized by the total cantilever length $L$. The contact wavenumber $\lambda_n L = \lambda_n^0 L\sqrt{\frac{f_n^c}{f_n^0}}$, where $\lambda_n^0 L$ is the free wavenumber given by the $n$th root of equation (2). The value of $D$ is given by

$$\begin{aligned} D = &\left[\sin\lambda_n L(1-\gamma)\cosh\lambda_n L(1-\gamma)\right. \\ &\left.-\cos\lambda_n L(1-\gamma)\sinh\lambda_n L(1-\gamma)\right] \\ &\times\left[1 - \cos\lambda_n L\gamma\cosh\lambda_n L\gamma\right] \\ &-\left[\sin\lambda_n L\gamma\cosh\lambda_n L\gamma - \cos\lambda_n L\gamma\sinh\lambda_n L\gamma\right] \\ &\times\left[1 + \cos\lambda_n L(1-\gamma)\cosh\lambda_n L(1-\gamma)\right]. \end{aligned} \quad (4)$$

There are various methods to implement equation (3). This can involve a rigorous model, where the tip-offset $\gamma$ is measured from the geometry, and the frequency-spacing of

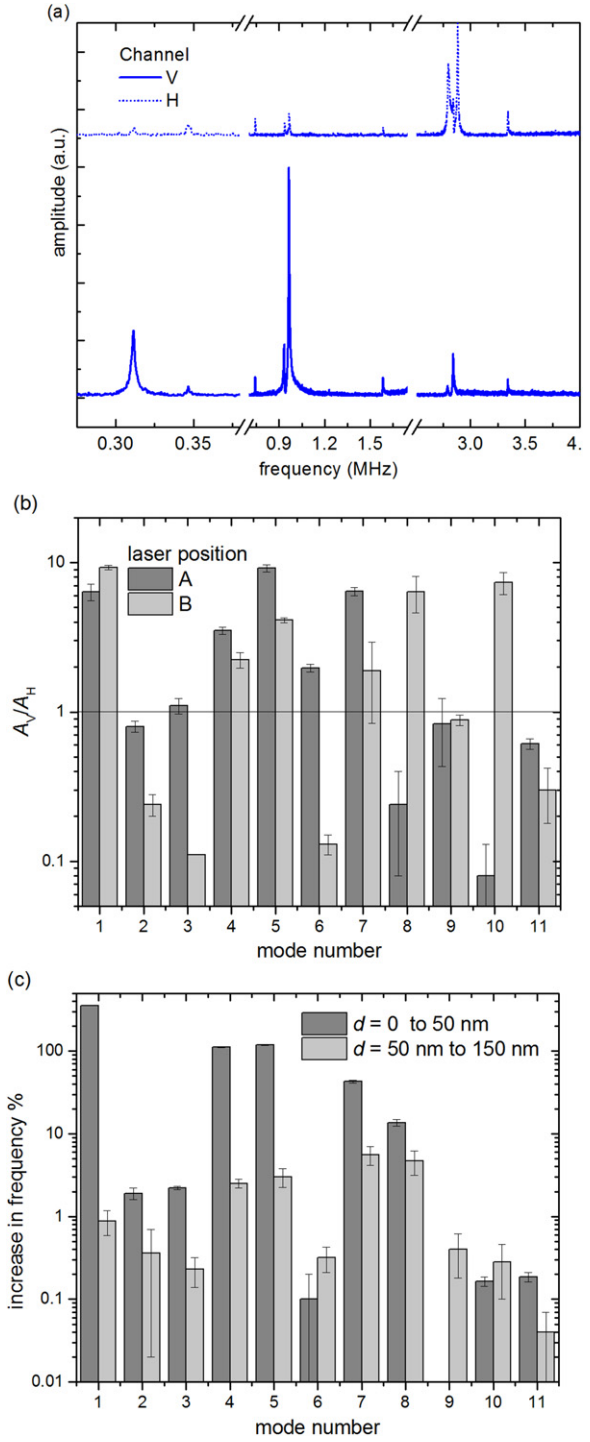


**Figure 6.** (a) Contact resonance spectra for vertical and horizontal photodiode (PD) channels with laser position B and setpoint deflection $d = 150$ nm. (b) Relative amplitude $A_V/A_H$ of vertical and horizontal channels for laser positions A and B. (c) Increase in frequency from free space ($d = 0$) to lighter contact ($d = 50$ nm) and from lighter contact ($d = 50$ nm) to harder contact ($d = 150$ nm). Error bars determined from the standard deviation of three measurements.

the free modes is derived from equation (1). Or, in the approach used here, the FEA-simulated free frequencies for each eigenmode are input into equation (3), rather than forcing the theoretical spacing. As a result, this 'scaled SAM' will necessarily converge to the free frequency of a given eigenmode as $\alpha \to 0$. For the scaled SAM analysis, the parameters $\gamma$ and $\alpha$ are simultaneously calculated with a 'mode crossing' approach using resonance frequency measurements or FEA modal simulations for two adjacent flexural eigenmodes with the same stiffness boundary conditions (i.e., on the same material at the same applied force or in the case of FEA with the same boundary springs) [33, 34]. Because the contact stiffness is nominally the same regardless of eigenmode and ignoring any frequency dependence, the value of $\gamma$ that yields the same value of $\alpha$ for both eigenmodes is taken as the solution. This approach has proven quite useful and accurate for analysis of rectangular cantilevers where the required rescaling is small, and the adjustable $\gamma$ parameter accounts for the variable-cross-section picket shape at the cantilever end.

Figure 7(b) shows the agreement between the scaled SAM model and the FEA model. The accuracy of the models is evaluated from the parameter

$$\Lambda = \left| \frac{\alpha_{\mathrm{FEA}} - \alpha_{\mathrm{ana}}}{\alpha_{\mathrm{FEA}}} \right|, \tag{5}$$

where $\alpha_{\mathrm{FEA}}$ is the prescribed stiffness in the simulation, and $\alpha_{\mathrm{SAM}}$ is the stiffness determined from the SAM model using the FEA contact resonance frequencies as inputs. Inputting frequencies for modes 1 and 2 in the scaled SAM provides excellent agreement at low to medium contact stiffness, with less than 1% disagreement up to a normalized contact stiffness $\alpha = 50$. Above $\alpha = 50$, the accuracy rapidly decreases. This onset for the decrease in accuracy likely results from the influence of lateral spring stiffness and finite tip height, which is included in the FEA but not in the SAM [29]. The analytical model could likely be made more accurate by including tip height and lateral stiffness; however, this introduces a number of additional model parameters that are not well known experimentally (e.g., Poisson's ratio). The lateral stiffness dominates the resonance frequency shifts when the normal stiffness approaches the pinned boundary condition limit. For rectangular cantilevers we have previously shown that, for increasing normal stiffness, the lateral stiffness and tip height effects are less consequential for higher eigenmodes that exhibit a higher dynamic stiffness [33]. The result is that the contact stiffness range for accurate analysis with the SAM model can be significantly extended by operating with the higher modes. For the HT-AFM cantilever, this is apparent in the accuracy results for modes 2 and 3, where less than 10% discrepancy is observed from $1 \leqslant \alpha \leqslant 550$. However, changing the analysis to include the third and fourth modes does not continue to increase the accurate stiffness range of the SAM model as was the case for rectangular cantilevers. The fact that no positive shift in the accurate contact stiffness range for good agreement between SAM and FEA occurs when moving to modes 3 and 4 from modes 2 and 3 suggests that unmodelled lateral stiffness effects are no longer the dominant source of error. For comparison, when tip height and lateral stiffness are added to the SAM model of the fourth eigenmode, there is less than a 1% effect on resonance

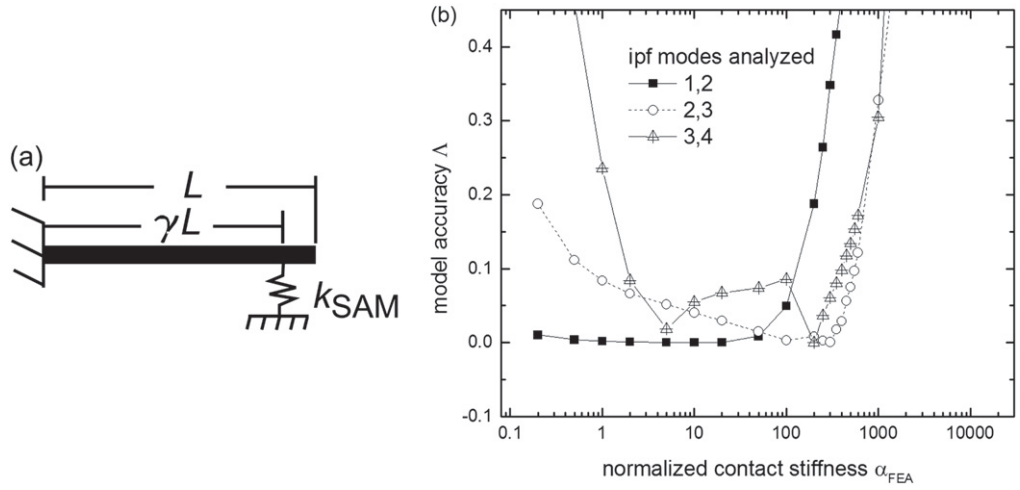


**Figure 7.** (a) Schematic of the simple analytical model (SAM). (b) Comparison of SAM results to those from FEA for a range of contact stiffness and eigenmodes. Model accuracy $\Lambda$ is defined in text.

frequency compared to the simpler model up to $\alpha = 2700$. But, when comparing the SAM results to HT-AFM FEA for modes 3 and 4, errors greater than 10% are observed when $\alpha > 450$. Thus, it seems likely that specific characteristics of the HT-AFM cantilever such as the non-constant cross section, stiffness of the cross member, and the observed anticlastic curvature require a model more advanced than a single distributed mass beam [32].

In practice, these results suggest that caution must be exercised in the quantitative calculation of contact stiffness from conventional beam models when the contact stiffness is much greater than the HT-AFM cantilever spring constant (i.e., $\alpha \gg 1$). Additional model development is required to achieve an accurate model over a wider stiffness range. This additional development could prove important, given proposed thermomechanical characterization methods that produce large non-Hertzian contact areas and hence high $\alpha$ values [7, 8]. Further model development may also yield quantitative analytical models of the other vibrational modes of the HT-AFM cantilever that have potential uses for measurement of in-plane shear properties.

## 4. Conclusion

With a combination of finite-element analysis and experiments, we have shown that commercial U-shaped AFM cantilevers with integrated heaters can exhibit a large number of vibrational modes within typical AFM frequencies as a result of the separate arms and coupling member. To identify these modes experimentally may require vibrational spectra from both horizontal and vertical photodiode channels, with optimally chosen laser positioning on the cantilever. The frequency spacing of flexural resonances where both arms vibrate in phase is slightly different from that predicted by Euler–Bernoulli theory for a beam with uniform cross section. Nonetheless, these modes exhibit sensitivity to changes in contact stiffness or force gradient qualitatively similar to the sensitivity of rectangular levers. The predominant new mode type introduced by the HT-AFM geometry is characterized by the *opF* motion of the arms. These modes appear relatively insensitive to contact stiffness for lower eigenmodes, but the higher eigenmodes show significant sensitivity at higher contact stiffness. Quantitative analysis of contact stiffness with analytical models was assessed with FEA data to simulate real contact resonance experiments. It was found that a simple beam model with only two parameters could predict the contact stiffness within 10% of the FEA model as long as an appropriately stiff eigenmode was used, and the contact stiffness was less than 500 times larger than the cantilever spring constant. More accurate analysis of contact stiffness could potentially be achieved by engineering HT-AFM cantilevers with geometry that is more readily reduced to Euler–Bernoulli segments. Additional design modifications could also be used to better separate the in-phase and out-of-phase modes to ease mode identification and assist in eigenmode tracking.

## Acknowledgments

This work was performed while R C Tung held a National Research Council Associateship Award at NIST. We thank C B Prater (Anasys Instruments) and J A Turner (University Nebraska–Lincoln) for valuable discussions.

## References

[1] Kajiyama T, Tanaka K, Ohki I, Ge S-R, Yoon J-S and Takahara A 1994 Imaging of dynamic viscoelastic properties of a phase-separated polymer surface by forced oscillation atomic force microscopy *Macromolecules* **27** 7932–4

[2] McGuiggan P M and Yarusso D J 2004 Measurement of the loss tangent of a thin polymeric film using the atomic force microscope *J. Mater. Res.* **19** 387–95

[3] Yang N, Wong K K H, Bruyn J R D and Hutter J L 2009 Frequency-dependent viscoelasticity measurement by atomic force microscopy *Meas. Sci. Technol.* **20** 025703
[4] Proksch R and Yablon D G 2012 Loss tangent imaging: theory and simulations of repulsive-mode tapping atomic force microscopy *Appl. Phys. Lett.* **100** 073106
[5] Ellison C J and Torkelson J M 2003 The distribution of glass-transition temperatures in nanoscopically confined glass formers *Nat. Mater.* **2** 695–700
[6] Cappella B, Kaliappan S K and Sturm H 2005 Using AFM force–distance curves to study the glass-to-rubber transition of amorphous polymers and their elastic–plastic properties as a function of temperature *Macromolecules* **38** 1874–81
[7] Jesse S, Nikiforov M P, Germinario L T and Kalinin S V 2008 Local thermomechanical characterization of phase transitions using band excitation atomic force acoustic microscopy with heated probe *Appl. Phys. Lett.* **93** 073104
[8] Nikiforov M P, Jesse S, Morozovska A N, Eliseev E A, Germinario L T and Kalinin S V 2009 Probing the temperature dependence of the mechanical properties of polymers at the nanoscale with band excitation thermal scanning probe microscopy *Nanotechnology* **20** 395709
[9] Haugstad G, Gladfelter W L, Weberg E B, Weberg R T and Jones R R 1995 Probing molecular relaxation on polymer surfaces with friction force microscopy *Langmuir* **11** 3473–82
[10] Dinelli F, Buenviaje C and Overney R M 2000 Glass transitions of thin polymeric films: speed and load dependence in lateral force microscopy *J. Chem. Phys.* **113** 2043–8
[11] Hobbs J K and Miles M J 2000 Direct observation of polyethylene shish-kebab crystallization using *in situ* atomic force microscopy *Macromolecules* **34** 353–5
[12] Schönherr H, Bailey L E and Frank C W 2001 Analyzing the surface temperature depression in hot stage atomic force microscopy with unheated cantilevers: application to the crystallization of poly(ethylene oxide) *Langmuir* **18** 490–8
[13] Hammiche A, Bozec L, Conroy M, Pollock H M, Mills G, Weaver J M R, Price D M, Reading M, Hourston D J and Song M 2000 Highly localized thermal, mechanical, and spectroscopic characterization of polymers using miniaturized thermal probes *J. Vac. Sci. Technol.* B **18** 1322–32
[14] King W P, Kenny T W, Goodson K E, Cross G, Despont M, Durig U, Rothuizen H, Binnig G K and Vettiger P 2001 Atomic force microscope cantilevers for combined thermomechanical data writing and reading *Appl. Phys. Lett.* **78** 1300–2
[15] King W P 2005 Design analysis of heated atomic force microscope cantilevers for nanotopography measurements *J. Micromech. Microeng.* **15** 2441–8
[16] King W P, Saxena S, Nelson B A, Weeks B L and Pitchimani R 2006 Nanoscale thermal analysis of an energetic material *Nano Lett.* **6** 2145–9
[17] Killgore J P and Overney R M 2008 Interfacial mobility and bonding strength in nanocomposite thin film membranes *Langmuir* **24** 3446–51
[18] Vettiger P *et al* 2002 The 'millipede'—nanotechnology entering data storage *IEEE Trans. Nanotechnol.* **1** 39–55
[19] Nelson B A and King W P 2007 Measuring material softening with nanoscale spatial resolution using heated silicon probes *Rev. Sci. Instrum.* **78** 023702
[20] Tovee P, Pumarol M, Zeze D, Kjoller K and Kolosov O 2012 Nanoscale spatial resolution probes for scanning thermal microscopy of solid state materials *J. Appl. Phys.* **112** 114317
[21] Nelson B A and King W P 2007 Temperature calibration of heated silicon atomic force microscope cantilevers *Sensors Actuators* A **140** 51–9
[22] García R and Perez R 2002 Dynamic atomic force microscopy methods *Surf. Sci. Rep.* **47** 197–301
[23] Maivald P, Butt H J, Gould S A C, Prater C B, Drake B, Gurley J A, Elings V B and Hansma P K 1991 Using force modulation to image surface elasticities with the atomic force microscope *Nanotechnology* **2** 103–6
[24] Rabe U, Amelio S, Kopycinska M, Hirsekorn S, Kempf M, Goken M and Arnold W 2002 Imaging and measurement of local mechanical material properties by atomic force acoustic microscopy *Surf. Interface Anal.* **33** 65–70
[25] Killgore J P, Yablon D G, Tsou A H, Gannepalli A, Yuya P A, Turner J A, Proksch R and Hurley D C 2011 Viscoelastic property mapping with contact resonance force microscopy *Langmuir* **27** 13983–7
[26] Lee B, Prater C B and King W P 2012 Lorentz force actuation of a heated atomic force microscope cantilever *Nanotechnology* **23** 055709
[27] Lee J, Beechem T, Wright T L, Nelson B A, Graham S and King W P 2006 Electrical, thermal, and mechanical characterization of silicon microcantilever heaters *J. Microelectromech. Syst.* **15** 1644–55
[28] Espinoza-Beltran F J, Geng K, Muñoz Saldaña J, Rabe U, Hirsekorn S and Arnold W 2009 Simulation of vibrational resonances of stiff AFM cantilevers by finite element methods *New J. Phys.* **11** 083034
[29] Wright O B and Nishiguchi N 1997 Vibrational dynamics of force microscopy: effect of tip dimensions *Appl. Phys. Lett.* **71** 626–8
[30] Huang L and Su C 2004 A torsional resonance mode AFM for in-plane tip surface interactions *Ultramicroscopy* **100** 277–85
[31] Turner J A and Wiehn J S 2001 Sensitivity of flexural and torsional vibration modes of atomic force microscope cantilevers to surface stiffness variations *Nanotechnology* **12** 322–30
[32] Rezaei E and Turner J A 2014 Free vibrations of U-shaped atomic force microscope probes *J. Appl. Phys.* **115** 174302
[33] Killgore J P and Hurley D C 2012 Low-force AFM nanomechanics with higher-eigenmode contact resonance spectroscopy *Nanotechnology* **23** 055702
[34] Rabe U, Amelio S, Kester E, Scherer V, Hirsekorn S and Arnold W 2000 Quantitative determination of contact stiffness using atomic force acoustic microscopy *Ultrasonics* **38** 430–7